Pergamon

Int. J. Multiphase Flow Vol. 22, No. 2, pp. 285–306, 1996

0301-9322(95)00070-4
0301-9322/96 $15.00 + 0.00

EFFECTS OF PARTICLE ARRANGEMENTS ON THE DRAG FORCE OF A PARTICLE IN THE INTERMEDIATE FLOW REGIME

S.-C. LIANG, T. HONG and L.-S. FAN†
Department of Chemical Engineering, Ohio State University, Columbus, OH 43210, U.S.A.

(*Received 6 May 1994; in revised form 5 October 1995*)

Abstract—The drag force of a single particle in the presence of other equal-sized particles arranged in specific configurations is measured directly for Re from 30 to 106. Four particle arrangements are investigated: a two-particle configuration (Model I), a three-coaligned particle configuration (Model II), a hexagonal particle configuration (Model III) and a cubic particle configuration (Model IV). Variables studied include the particle Reynolds number (Re) and the separation distance. The effect of pipe wall on the measurement results is also examined. The measured drag force, expressed in terms of the drag ratio, is compared with the theoretical values at zero Re and the experimental values for $100 < Re < 10^3$ reported in the literature. Comparisons of the experimentally determined drag ratios with numerically simulated values are also conducted. Because of the Re effect, the drag ratio curves for Model I are no longer symmetrical with respect to $\theta = 90°$ as observed for the Stokes flow. The results for Model I at $\theta = 90°$ show that the drag ratio increases with the separation distance and then decreases with further increasing separation distance, and the combination of the Re and wall effects causes the drag ratios higher than unity. For Model II, the drag ratio of the middle particle is lower than that of the upper particle at small separation distances but becomes slightly higher beyond a certain separation distance. The computational results provide detailed information on the flow field around each particle, and the pressure and the shear stress distributions on particle surfaces. The numerically simulated drag ratios compare reasonably well with the experimental data. The drag ratio behavior for Model IV is found to be similar to Models I and III; however, the Re does not seem to affect the drag ratio. The results of the flow visualization conducted in this study clearly demonstrate a significant change of the wake structure of Models I and III at different separation distances.

Key Words: drag force, particle arrangement, separation distance, Re effect, wall effect, intermediate flow regime, flow field

1. INTRODUCTION

The knowledge of the particle drag force is important in the flow analysis of particulate and multiphase flow systems. For an isolated particle or for particles in dilute systems, the particle drag force can be obtained theoretically or semi-empirically. However, in concentrated particulate systems, particle interactions become important and thus the particle drag force in these systems may deviate significantly from that of an isolated particle. A fundamental requirement to fully quantify the drag force effects in concentrated particulate systems is to understand the drag behavior of a single particle in the presence of other particles.

In the determination of the particle drag force, the most commonly used approach is to measure the pressure drop and convert it to an average drag force of a single particle. For flows through a packed bed of particles, the particle drag force can be correlated as a function of voidage and particle Reynolds number (Re) using the Ergun equation (Soo 1990). A similar approach measuring average drag forces of an assembly of fixed particles has been done for dilute systems. Happel & Epstein (1954) employed a simple cubic particle configuration as a model to study the relationships between the pressure drop and the voidage in the Stokes flow regime. Stinzing (1971) and Tsuji *et al.* (1985) conducted similar experiments with particles suspended in a pipe; the flows investigated were in the turbulent flow regime. In the work of Stinzing (1971), the particles were cylindrical in shape and the rods supporting these particles were placed vertically. They found that the drag of particles in the assembly was smaller than that of an isolated particle, which was in contrast to

†Author for correspondence.

the general concept of particle drag force in a multi-particle flow system. Tsuji *et al.* (1985) reported that, in general, the particle drag coefficient was larger than that for the single case; however, the particle drag coefficient for the square grid model was found to decrease with increasing particle concentration. Because of the increase in the turbulent intensity induced by the horizontally-placed supporting rods, the values of particle drag force obtained by Tsuji *et al.* (1982) are higher than those obtained by Stinzing (1971). It is noted that the expression used by Stinzing for the overall drag force on the particles, as related to the pressure drop ΔP, is $F_D = \Delta P \bullet A \bullet \epsilon$, which is in contrast to the common expression $F_D = \Delta P \bullet A$ where A is the cross-sectional area of the pipe and ϵ is the bed voidage.

The theoretical analysis of particle drag force has also been performed for flow through assemblages of spheres. LeClair & Hamielec (1968) solved the Navier–Stokes equation for flow in the intermediate Re regime by employing a surface-interaction model to account for particle interactions. The comparison between their model prediction and the data obtained from the Ergun equation showed agreement within 15%; however, there was a significant discrepancy at higher Re. Jaiswal & Sundararajan (1991) conducted similar studies using a finite element technique over wider ranges of voidages and Re ($0.3 \leq \epsilon \leq 0.9$ and $10^{-3} \leq \mathrm{Re} \leq 100$). The advantage of the surface-interaction model is that it can reduce the multiparticle flow problem to a single particle one; however, such a simplification cannot account for the difference in the drag force between individual particles. In general, none of the above methods can provide complete and rigorous information on the particle drag force in particulate systems.

The major research effort on the study of the drag force of individual interacting particles has mainly focused on unbounded Stokes flows (Happel & Brenner 1983; Batchelor 1982; Brady & Bossis 1988). Happel & Brenner (1983) employed a scheme of successive iterations to solve the Navier–Stokes equations for flows past two particles. They reported that for all the centerline orientations the particle drag force is lower than that of a single particle. Kim (1987) used the addition theorems to analytically solve the Stokes flow past three spheres arranged in an equilateral triangle on a plane perpendicular to the flow. The experimental work on three-particle interactions has also been limited to Stokes flows and well-separated three-sphere clusters. One important development in theoretical studies on the many-body problem is the Stokesian dynamics approach, which dynamically simulates the behavior of a large number of particles in an unbounded flow (Brady & Bossis 1988; Fuentes & Kim 1992). This technique can also be applied to bounded flows and flows past fixed particles. Brady & Bossis (1988) reported that the prediction of the drag coefficients of seven particles in an arrangement perpendicular to its centerline agrees very well with the results obtained by Ganatos *et al.* (1978). Another important aspect in the study of the drag force of interacting particles is the wall effect. Also, the majority of these studies have been limited to Stokes flows. Goldman *et al.* (1966) studied two particles settling side-by-side in a cylinder. Their results showed that to the approximation of the first power of particle-to-pipe diameter ratio, the presence of the wall effect resulted in an increase in the drag force by 2% for a particle-to-pipe diameter ratio of 0.0182.

Outside the Stokes flow regime, there have been only a few fundamental studies dealing with the drag force of a small number of particles; consequently, our understanding is very poor. Lee (1979) and Tsuji *et al.* (1982) conducted experiments on the interactions between two particles at Re of about 10^4 and Re from 100 to 10^3, respectively. Their results showed that the drag force of the trailing particle decreased with decreasing distance between particles, but the particle drag force increased as the other particle approached from the transverse direction. For lower Re, Rowe & Henwood (1961) presented a diagram of drag ratios versus angular displacement at three different separation distances for $\mathrm{Re} = 96$. Recently, Zhu *et al.* (1994) used a micro-balance to measure the drag force on two interacting particles arranged in the longitudinal direction for Re from 20 to 130. They reported a similar trend in the drag ratio versus separation distance for the trailing particle and a unique crossing phenomenon where drag ratio curves cross each other at a separation distance of about 1–3 particle diameters. There was, however, only a slight decrease in the drag ratio for the leading particle. The Re was found to affect not only the magnitude of the drag ratio but also its variation with the distance between particles.

Because of the complex coupling of both the viscous and inertial effects, the theoretical studies on particle drag force in the intermediate flow regime has focused on the numerical simulation.

Some simulation work can be found in the studies to predict the heat and mass transfer characteristics of fuel droplets (Taniguchi & Asano 1987; Tal *et al.* 1984). Kim *et al.* (1993) obtained three-dimensional numerical simulations for flows past two particles placed next to each other at Re = 50, 110 and 150. They found that the drag coefficient decreased with increasing separation distance, and increased slightly as the separation distance further increased, and gradually leveled off to the value for an isolated particle. For more concentrated systems, the particle interaction usually involves more than two particles. Ramachandran *et al.* (1991) used a finite element method to solve the Navier–Stokes equations for a steady laminar axisymmetric flow past three spheres for Re from 1 to 200. The centerline of the three particles is parallel to the flow direction, and the distances between the center particle and the outer two particles were varied independently from two to six particle diameters. It should be noted that the separation distance, x, defined in this study is based on the distance between the particle surfaces; whereas the separation distance in the study of Ramachandran *et al.* (1991) was defined based on the distance between the particle centers. For the case where three particles are equally-spaced and the separation distances are two particle diameters, a change in the order of the drag ratio was observed for the two downstream particles. Rowe (1961) studied the effect of particle concentration on the drag force of particles arranged in a hexagonal pattern for Re from 32 to 96. He reported that the drag ratio of a particle in the array to that of an isolated particle increased with decreasing separation distance and that there was no significant dependence of the particle drag ratio on Re.

In general, the drag force of particles in a bounded flow is governed by the number of surrounding particles, the particle separation distance, the relative position of the particles, the Re and the presence of the pipe wall. The purpose of this study is to examine the effects of the above parameters on the behavior of the drag force of a small number of particles in the intermediate flow regime. This study can serve as a first step towards understanding more complex and realistic situations, and can also be used to validate numerical schemes. The drag force of a single particle is measured in the presence of other particles arranged in different configurations. The wall effect is investigated by varying the size of particles while keeping the size of the circulation pipe constant. One significance of the flow structure at these Re is the formation of a wake; therefore, the flow visualization on the wake interaction around particles is carried out. In addition, a detailed flow field for the three-coaligned particle configuration is obtained from the numerical simulation. The experimental results of the particle drag force are compared with both the theoretical results obtained at low Re and the simulation results.

2. EXPERIMENTAL

A schematic diagram of the experimental apparatus is shown in figure 1. The experiments are performed in a Plexiglas pipe of 15.24 cm i.d. and 228.6 cm height. A glycerin/water solution of approximately 82 wt% glycerin is circulated upwards through the pipe. With this viscous fluid, the drag force acting on the particle can be increased to the accurately detectable range of the micro-balance, which has the resolution of 1 mg. For example, at the temperature of 20°C, the micro-balance measures the particle drag force of 486 mg at Re = 71. Since the viscosity, μ, of the glycerin solution varies significantly with temperature, the fluid temperature is maintained constant throughout the experiments. The fluid viscosity is measured using a Fann series 35 rotational viscometer.

The liquid velocity is obtained by measuring the velocity of tiny bubbles that are present in the fluid. The approximation of the fluid velocity by the bubble velocity has been validated by Zhu *et al.* (1994). To obtain the bubble location on the centerplane of the pipe, two vertical collimated light sources are placed 180° apart outside the circumference of the pipe. Since the light sheet is very narrow, the bubbles moving upwards on the centerplane of the pipe appear brighter than the rest of the bubbles and therefore can be identified. The movement of bubbles is video recorded at a rate of 60 frames/s and their locations can be determined from a scale marked on a T.V. screen, whose relationship with the actual dimension is predetermined. For the calculation of the Re for all particle arrangements, the fluid velocity is obtained by averaging the bubble velocities at four evenly-spaced radial locations from the left to the right edges of the test particle. The bubble velocity at each location is an average value for four sets of bubble velocities. The average fluid

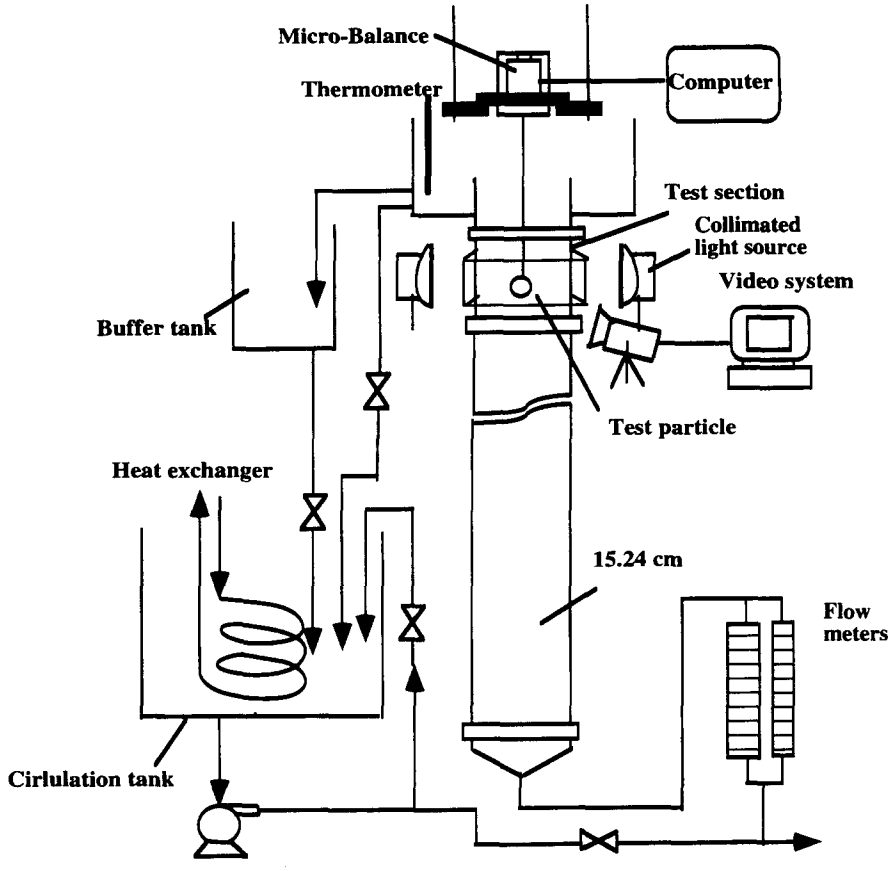

Figure 1. Schematic diagram of the experimental apparatus.

velocity, $\bar{U}$, determined in this manner ranges from 10 to 37 cm/s. Brass spheres of three different diameters, d, are used in this study: 1.27, 1.58 and 1.91 cm. The experiments are carried out for $\mathrm{Re}(=d\bar{U}\rho/\mu)$ from 29 to 106 where ρ is the fluid density. The number of surrounding particles and the separation distances considered vary from 1 to 8 and 0 to 7 particle diameters, respectively. The separation distance, l, is defined as the distance between the particle surfaces as shown in figure 2.

The method used to measure the drag force of the test particle is given in Zhu *et al.* (1994). Briefly, the test particle is attached to an electronic balance through a thin rod such that the drag force acting upward on the test particle can be measured. Drag force measurements are conducted on the test particle attached to the rod and on the rod only. The particle drag force can be obtained

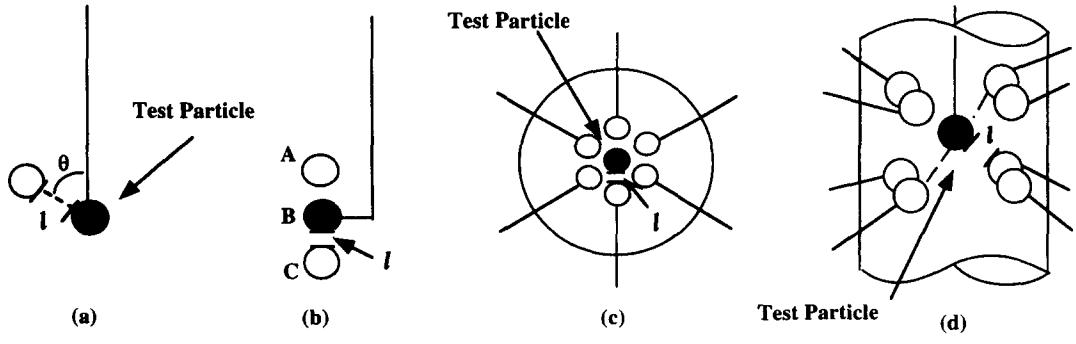

Figure 2. Particle arrangements: (a) two-particle configuration (Model I); (b) three-coaligned particle configuration (Model II); (c) hexagonal particle configuration (Model III); and (d) cubic particle configuration (Model IV).

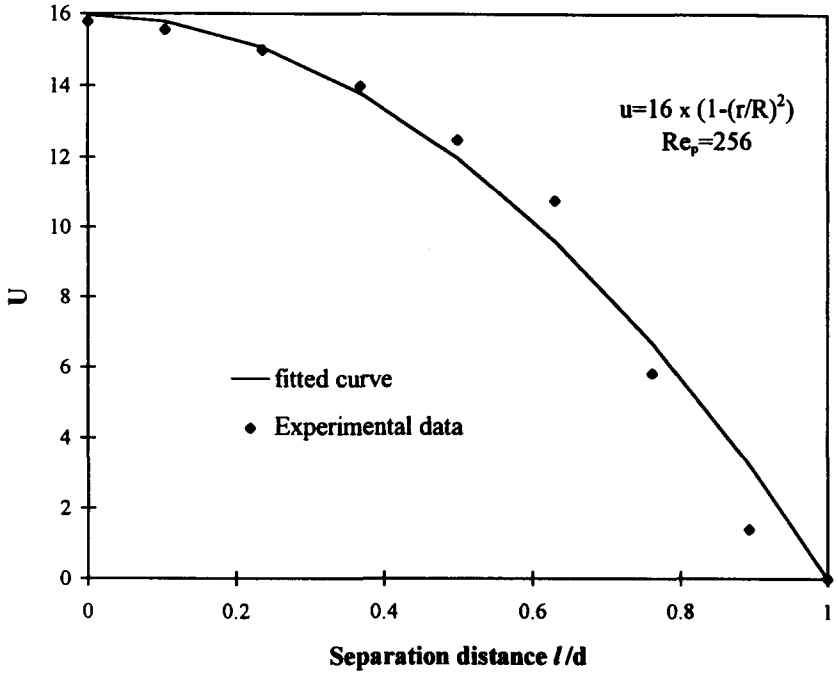

Figure 3. Velocity distribution along the radial direction at $Re_p = 256$.

by subtracting the drag force of the rod from that of the test particle with the rod. Since the drag force of the rod is also a function of the particle arrangement, its value is obtained from separate measurement for each particle arrangement.

Four types of particle arrangements, shown in figure 2(a)–(d), are investigated in this study: a two-particle configuration (Model I), a three-coaligned particle configuration (Model II), a hexagonal particle configuration (Model III) and a cubic particle configuration (Model IV). In Model I, the centerline of the two particles is arranged at five different orientations with respect to the flow direction. In Model II, three particles are arranged along the pipe centerline and each particle is fixed in space by rods inserted from the top of the pipe. The two surrounding particles are attached to dial calipers, which allow the adjustment of the spacing between the test particle and the surrounding particles. In Models I, III and IV, the surrounding particles are also held in the test section independently and are positioned by rods penetrating through the test section. The distance between particles can be adjusted by altering the depth of the rod into the pipe. In Model III, six particles are arranged on the vertices of a hexagon and the supporting rods are placed horizontally. In this case, the plane of the centers of the particles is normal to the flow direction. In order to arrange eight particles into a simple cube, the supporting rods for Model IV are placed 53° from the pipe centerline.

To study the interaction between the wakes among particles, the streamlines around the particles are obtained photographically from short-time exposure of bubbles and from video recordings of the bubble movement. A rectangular viewing window made of Plexiglas and filled with glycerin solution identical to the circulating fluid is used for the flow visualization. The location of the vertical illuminated plane is determined based on the significance of the wake interaction. For Model I, the illuminated plane passes through the centers of both particles and for Model III it passes through the centers of the test particle and any two surrounding particles that are 180° apart. Such an arrangement is intended for visualization of the wake interaction on the plane where the particle interaction becomes most pronounced. Because of the arrangements of the particle assembly of Model IV and the viewing window, it is difficult to observe the flow field in the vicinity of the test particle; therefore, no photographs are provided for Model IV.

3. RESULTS AND DISCUSSION

3.1. Experimental results

Figure 3 shows a typical velocity distribution along the radial direction. The solid line represents the velocity profile of a fully developed laminar flow, which is constructed based on the average flow velocity calculated from the volume flow rate. In this case, the average flow velocity based on the cross-sectional area of the pipe is 8 cm/s, r is the distance from the pipe centerline and R is the pipe radius. The pipe Reynolds number (Re_p) based on this average flow velocity ranges from 180 and 636. The good agreement between the experimental data and the assumed velocity profile demonstrates that the pipe flow in the absence of particles is a Poiseuille type of flow.

Since the sizes of the particles and the pipe employed in these experiments are different from those in our earlier work (Zhu *et al.* 1994), a calibration of the drag force measurement system is conducted to validate this technique for the new system. The comparison of the drag coefficient of a particle from the experimental results with that from the literature demonstrates that the experimental data closely follow the standard drag curve. To report the variation of the drag force of the test particle, the drag force of the test particle (F_d) and the separation distance are normalized by the drag force of an isolated particle (F_{d0}) and the particle diameter, respectively. For each value of the drag ratio reported, the drag force of an isolated particle is obtained by direct measurement.

The drag ratios at various separation distances for three particle-to-pipe diameter ratios (d/D) for Model I at $Re_p = 222$ are shown in figure 4. The velocity profile of the incoming flow is the same for all three cases and the average velocity used to calculate Re is found to differ by less than 2% between the cases of $l/d = 0.08$ and 0.13. The drag ratio curves are characterized by an increase then a decrease with increasing separation distance. For comparison, the drag ratios for unbounded Stokes flows are also shown in figure 5. The significant difference in the shape of these two sets of drag ratio curves is mainly caused by the wall effect. In the absence of a wall, the flow encounters much more resistance within the gap and the flow tends to go around the two particles. This phenomenon becomes more significant when two particles are very close to each other as demonstrated by the drag ratios with values less than unity and the decreasing drag ratio with decreasing separation distance for the Stokes flow. When subjected to the wall effect, some of the

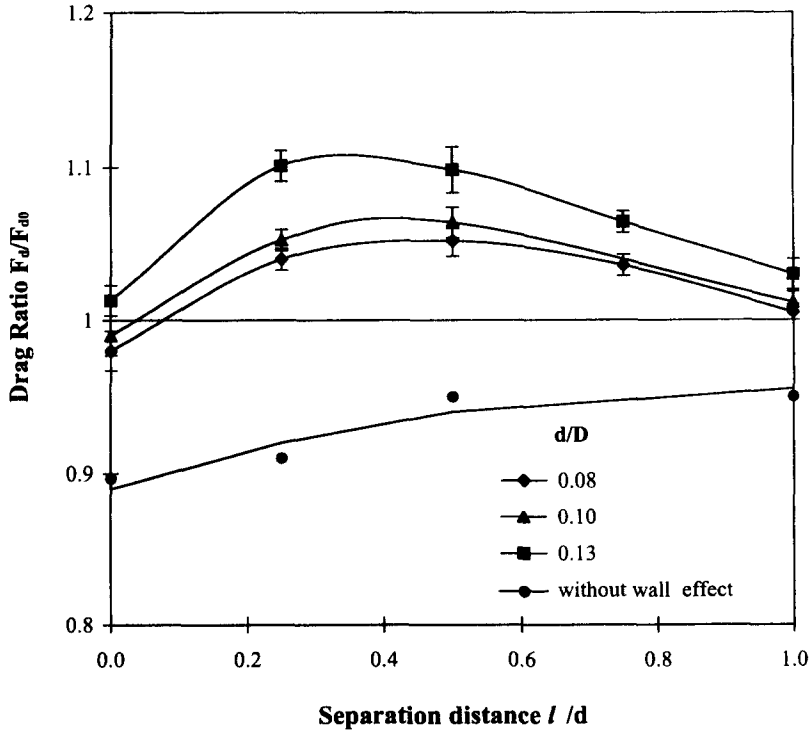

Figure 4. Variations in the drag ratios with separation distance for three particle-to-pipe diameter ratios for Model I ($\theta = 90°$).

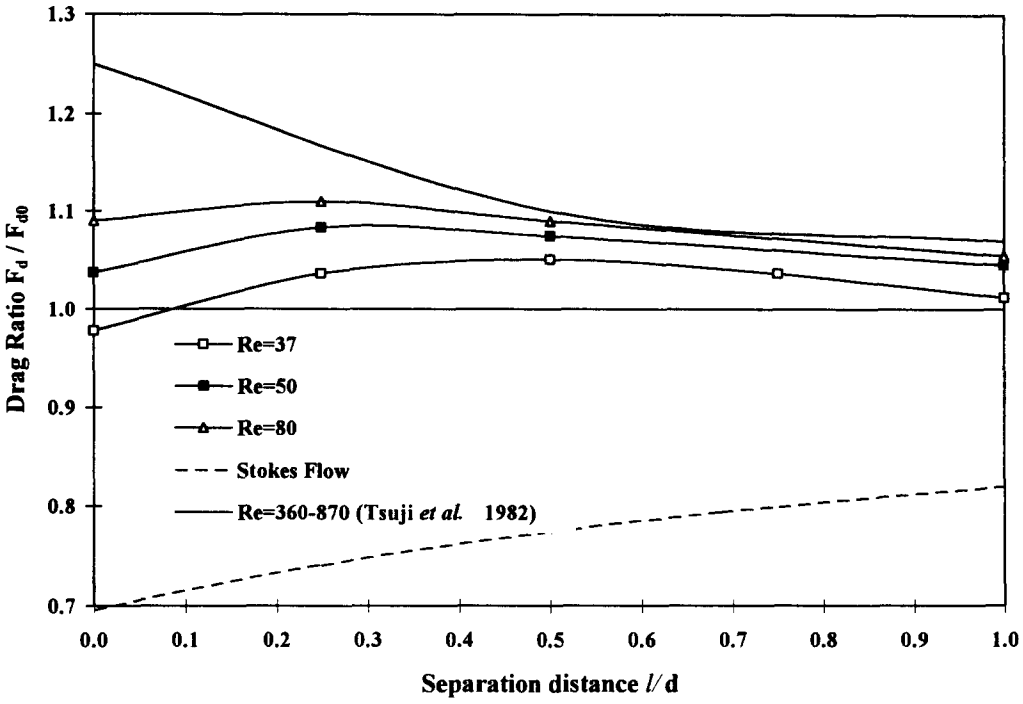

Figure 5. Variation in the drag ratio with separation distance at different Re for Model I (θ = 90°).

flow is forced to pass through the gap, which leads to a higher drag ratio. In contrast to Stokes flows, the majority of the drag ratios obtained in this Re range have values larger than unity. Compared with the drag force of a single particle, the higher drag force due to the presence of both the surrounding particle and the wall can be easily understood; however, it is unclear if the increase in the Re also contributes to the drag ratio with values larger than unity. In order to determine the Re contribution, one can examine the drag ratio in the absence of the wall effect by extrapolating the curve of drag ratio versus d/D to $d/D = 0$ with the assumption of a linear relationship between the two parameters. As shown in figure 4, in the absence of the wall, the estimated values of the drag ratios at $Re_p = 222$ are less than unity and they exhibit a trend similar to that for the Stokes flow. Consider the case for $l/d = 0$ and $d/D = 0.08$; one can find that the drag ratio increases from 0.7 to 0.9 as the Re_p increases from the zero Re range to 222, and it further increases up to 0.98 when subjected to the wall effect. Table 1 shows the comparison of the Re and wall effects for $l/d = 0.08$. The data in the second column represent the drag ratios without the wall effect divided by that for the Stokes flow. The data in the third column are obtained by dividing the drag ratio with the wall effect by that without the wall effect. It can be seen that at $Re_p = 222$, the 16–29% increase in the drag ratio is attributed to the Re effect and an extra 6–14% increase is observed when the wall effect is present.

The drag ratios of 1.27 cm particles at three Re: 29, 50 and 80, are shown in figure 5. The drag ratio curves of concave shape are also observed. The concave parts of the curves appear to gradually flatten out as the Re increases. For comparison, the results reported by Tsuji *et al.* (1982) and the theoretical values for the Stokes flow are also shown in the same figure. It is noted that the d/D in the study of Tsuji *et al.* (1982) ranges from 0.06 to 0.1, which is close to the value of

Table 1. Comparison of the Re effect with the wall effect for Model II at Re = 37 and θ = 90°

l/d	Re effect	Wall effect
0	1.29	1.09
0.25	1.23	1.14
0.5	1.23	1.11
1.0	1.16	1.06

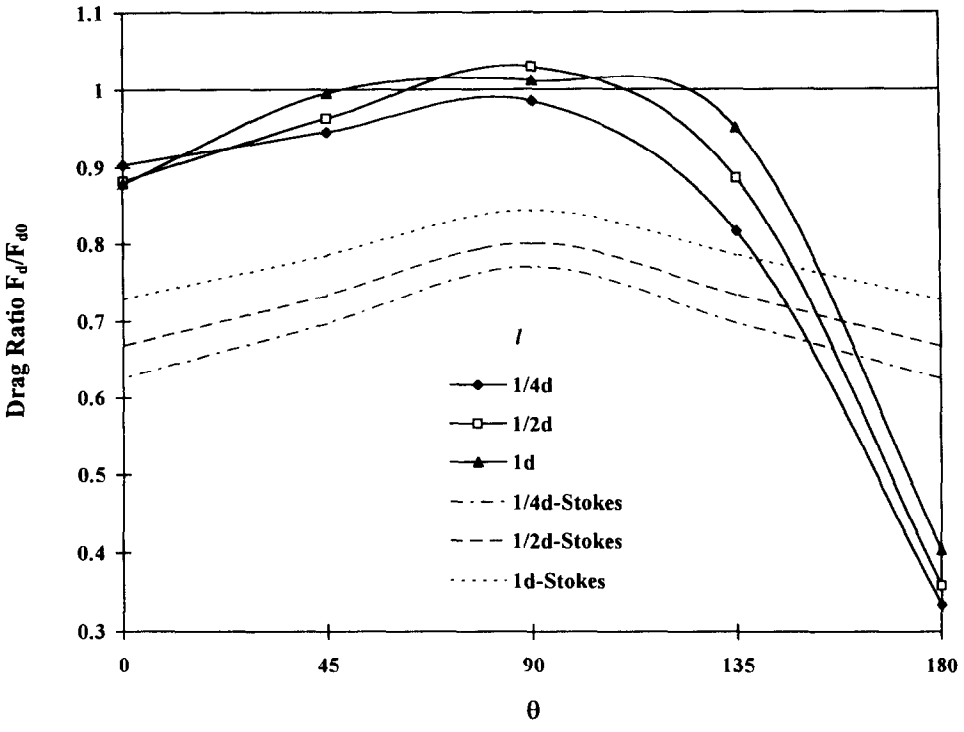

Figure 6. Drag ratios at various θ for Model 1.

d/D (=0.08) used in this study. Since their data are scattered and plotted on a semi-log scale, it is difficult to pinpoint the exact values of the drag ratio. Therefore, their data are presented in terms of a fitted curve. It is found that their data and the theoretical values at zero Re correspond to the upper and lower bounds, respectively, of the data obtained in this study; the former curve is of a concave shape and the latter is of a convex shape. Furthermore, as the Re increases, the drag ratio curves obtained move upwards and approach the one obtained by Tsuji *et al.* (1982). This trend can also be verified as follows: consider the two particles at zero separation as a single one of diameter $2d$. Since the wall effect has been known to become less significant as the Re increases (Ayukawa *et al.* 1970), one would expect a decrease instead of an increase in the drag ratio as the Re increases if the wall effect dominates. Therefore, it can be concluded that as the Re increases, the drag ratio increases. To determine if the drag ratio with values larger than unity is caused by the increase in the Re or the presence of the wall, one can consider again the two 1.27 cm particles for $l/d = 0$ in Tsuji *et al.*'s experiments as a 2.54 cm particle. The corresponding drag ratio in the presence of the wall is about 1.16 for $d/D = 0.2$ (Ayukawa *et al.* 1970); however, the drag ratio from the results of Tsuji *et al.* (1982) is about 1.3. This indicates that the Re effect can result in drag ratios larger than unity. It should be noted that there is vortex shedding in the flow they studied. The simulated drag coefficients at Re = 50 read from the figure of Kim *et al.* (1993) give drag ratios of 1.08 and 1.05 for $l/d = 0.5$ and 1, which agree with the results in the present study. This indicates that the wall effect is also significant in their simulation although there is essentially no difference in the drag coefficients of an isolated particle at both Re = 50 and 100 as the D/d increases from 10.5 to 16.5.

Figure 6 shows the variation of the drag ratio with the orientation of the surrounding particle for three separation distances at Re = 37. The corresponding particle drag ratios for the Stokes flow are also shown in figure 6. It is found that the symmetry of the drag ratio with respect to $\theta = 90^\circ$ found for the Stokes flow is distorted at this moderate Re. This important feature can be used to explain some phenomena associated with the dynamic motion of particles in this Re regime. For the Stokes flow, the two particles experience the same drag force regardless of their orientation; as a result, there is no relative motion between the two particles. At the intermediate

Re and $\theta = 45°$, the test particle is subject to a larger drag force than that of the surrounding particle, which consequently causes the relative motion between them.

It is found that the particle drag ratio has larger values than those in the Stokes regime except when the test particle is in the vicinity of the wake of the surrounding particle ($135° < \theta < 180°$). The drag behavior can be attributed to the combined effect of both the Re and the wall. The Re effect appears to be the predominant factor for the increase and decrease in the drag ratios compared with those for Stokes flows in the cases of $\theta = 0°$ and $\theta = 180°$, respectively. This can be explained as follows. It is reasonable to assume that the wall has an effect on the two particles equivalent to that on a single particle. Therefore, in these two cases, the wall effect can be neglected and the deviation of the drag ratios from those in the Stokes regime is primarily due to the Re effect. The significant reduction in the drag ratio at $\theta = 180°$ is the result of the wake effect.

For the Stokes flow, the particle drag ratio increases with increasing separation distance at all orientations for the two particles. The results obtained in this study, however, show that there are exceptions to this trend around $\theta = 0°$ and 90°. At $\theta = 0°$, the drag ratio initially decreases with increasing particle separation, then increases as the separation distance continues to increase and gradually approaches unity. More details can be found in Zhu *et al.* (1994). At $\theta = 90°$, the drag ratio increases with increasing separation distance and then decreases with further increase in the separation distance. As explained previously, this is caused by the wall effect.

It is noted that Rowe (1961) reported a monotonic increase or decrease in the drag ratio with the separation distance, although, in his experiment, the ratio of the particle diameter to the tank width is 0.08, which is the same as the condition used in this study. Another difference is that the drag ratios at both $\theta = 45°$ and 135° obtained in this study have values less than unity. In addition, the present results show that the drag ratios for $l/d = 0.25$ is lower than unity. This could be attributed to the lower Re (= 37) compared with the Re in his experiments (= 96).

The drag ratios of each particle and their sum at various separation distances for Model II are shown in figure 7. The particle diameter is 1.58 cm. The drag ratios of all three particles decrease monotonically with the separation distance. Particle C has the highest drag ratios; particles A and B have much lower drag ratios because of the wake effect. At small separation distances, the interaction effects cause particle B to have the largest drag reduction; however, as the separation distance increases to a value of 2–3, the drag ratio of particle B becomes larger than that of particle A but the difference between them is not very significant. This drag force behavior can be used to describe the relative motion of three equally-separated particles moving along their centerline at the same initial velocity. If the initial separation distance is larger than a certain value, particle A falls faster than particle B and gradually catches up with particle B, but at smaller separations, particle B falls faster than both particles A and C and eventually catches up with particle C. This phenomenon is also confirmed from the simulation results, which will be discussed later. It is of interest to compare our results with the theoretical ones obtained for Stokes flows. As shown in figure 7, the sum of the drag ratios of three particles for the Stokes flow (Happel & Brenner 1983) is higher than that obtained in this study.

Figure 8 shows the variation of the drag ratios of particle B with the separation distance at four Re for Model II. Similar to the results on the drag ratio of the trailing particle reported by Zhu *et al.* (1994), the drag ratio of particle B decreases with separation distance and reaches a minimum at zero separation; however, the drag ratios in this study have lower values than those in Zhu *et al.* (1994).

The trend of the drag ratio curves for Model III is similar to that for Model I. A maximum increase in drag ratio—40%—occurs for $l/d = 0.5$, and higher Re leads to more significant increase in the drag ratio (figure 9). It is also seen that the concave drag ratio curves gradually flatten out as the Re increases. This drag behavior is more difficult to explain because of the interaction of multiparticles and the interplay of the wall effect and the Re effect. It seems that the wall effect, leading to a great reduction in the cross-sectional area, is the main reason for the increase in the drag ratio.

Compared with the results of Rowe (1961), for $l/d > 0.5$, the trend of the drag ratios is the same and the values are of the same order of magnitude but slightly lower. It should be noted that there are several differences. In his experiments, there are more surrounding particles and therefore a significant increase in the linear flow velocity is expected. In addition, the planes of particles in

a hexagonal configuration were parallel, not perpendicular, to the flow direction, and the planes of all three layers of particles were placed 60° to the flow direction. These different particle arrangements can have significant effects on the values of the drag ratio and the smaller cross-sectional area can also result in an increase in the drag ratio.

Figure 10 shows the drag ratios of the test particle at four separation distances for Model IV. For small separation distances, it is found that the drag ratios increase with increasing separation distance and have values less than unity; however, for $l/d = 1$, the drag force of the test particle becomes larger than that of an isolated particle. This behavior can be explained in terms of the results shown in Figure 6. The arrangement of the surrounding particles in Model IV represent a combination of two types of Model I particle interaction: $\theta = 45°$ and 135°. Figure 6 shows that the drag ratios for both $\theta = 45°$ and 135° are less than unity. Therefore, the combined effect of four sets of these two interactions results in a further reduction in the drag ratio. For example, at Re = 37 and $l/d = 0.5$, the drag ratios are 0.96 and 0.88 for $\theta = 45°$ and 135°, respectively; the corresponding drag ratio for Model IV is 0.7. Unlike the previous models, the test particle and the surrounding particles interact in such a way that the Re has no significant influence on the drag ratio. This may be explained as follows. At $\theta = 135°$ where the test particle is in the vicinity of the wake of the surrounding particle, the drag ratio decreases with increasing Re similar to the case of $\theta = 180°$ (Zhu *et al.* 1994). On the other hand, at $\theta = 45°$, the drag ratio behavior is closer to the case of $\theta = 90°$ where the drag ratio increases with increasing Re. These two counteracting effects cancel each other, leading to the Re independence of the drag ratio for Model IV.

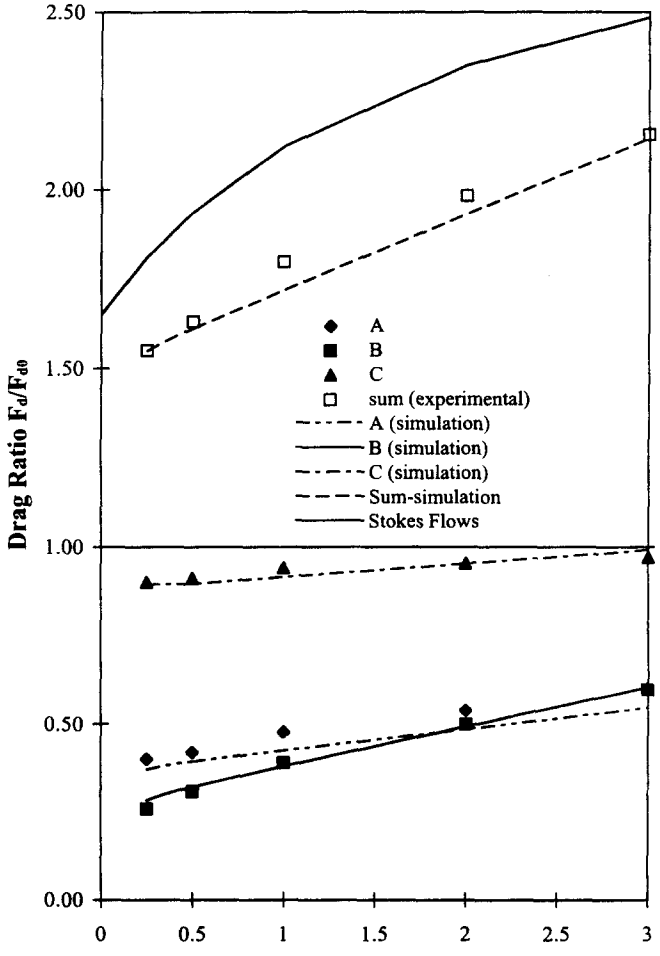

Figure 7. Drag ratios of particles and their sum for Model II.

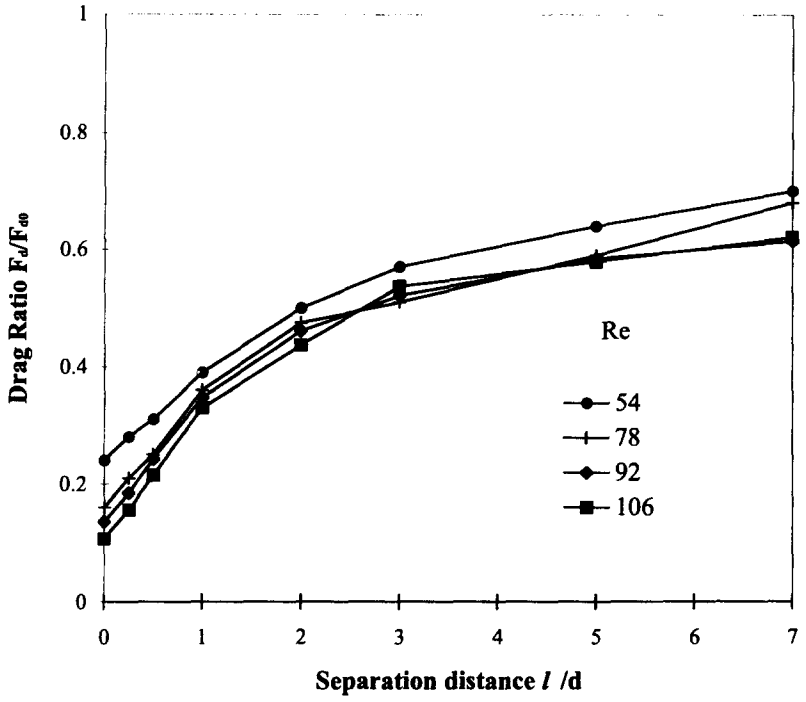

Figure 8. Variations in the drag ratio with the particle separation distance for particles in Model II.

3.2. Flow visualization

Figure 11(a)–(d) shows the flow field in the wake region for Model I with $\theta = 90°$ at Re = 60. The particle on the left-hand side is the test particle which is placed in the center of the pipe. For $l/d = 0$ [figure 11(a)], the vortex-rings of two particles merge into one large vortex-ring with a length of about 1.64 particle diameters. As the l/d increases to 0.25 [Figure 11(b)], a single vortex-ring is still observed but with a smaller length—1.4 particle diameters. Since the shutter speed is the same in all cases, the less-continuous streamlines for the case of $l/d = 0.25$ indicate a weaker circulation inside the wake. As the l/d further increases to 0.5 [figure 11(c)], the flow develops separate wakes behind each particle. The fluid particles outside (left-hand side) the test particle moves in an S-shaped path downstream and there is a small vortex attached to the outer edge of the particle. A similar phenomenon is found for the surrounding particles. As the l/d increases to 1.0 [figure 11(d)], this vortex becomes larger and another vortex forms downstream on the inner side of the test particle; the former vortex seems to be wider and longer than the latter. Also, the size of the wake of the test particle appears to be smaller than that of a single particle.

For Model III, for $l/d = 0.25$, one large vortex-ring forms downstream from the particle assembly as shown in figure 12(a). The centers of the vortex-ring are about 2.2 particle diameters away from the upper edge of the particles. It is noted that, unlike Model I, the flow passing through the gaps between the test particle and the surrounding particles moves in an S-shaped path around the bottom of the two vortices and is entrained by the flow outside of the particle assembly. Another difference is that a small vortex forms on the inner side of the surrounding particle for this model but on the outside of the surrounding particle for Model I.

For $l/d = 0.5$, the centers of the vortex-ring move further downstream and the two vortices become closer to each other [figure 12(b)]. In the case of $l/d = 1$ [figure 12(c)], the vortex-ring behind the test particle becomes larger; however, similar to Model I, its size seems smaller than that of a single particle.

3.2. Numerical simulation on Model II

In order to obtain detailed flow field and pressure distribution information for Model II, numerical simulations are conducted. Using the finite difference method and body-fitted coordinates, the complete momentum equations are solved for steady laminar axisymmetric

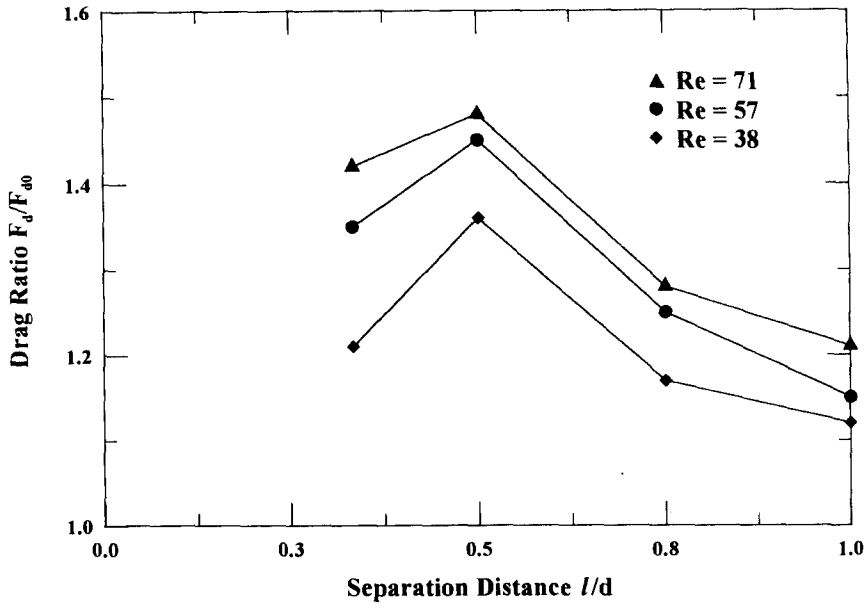

Figure 9. Relationships between the drag ratio and the particle separation distance for three Re values for Model III.

incompressible flow. In this study, as the Re is less than 110, the wake of the spherical particle is assumed to be steady.

3.3.1. Governing equations and boundary conditions. The continuity and the momentum equations for a steady laminar flow take the forms:

$$\nabla \cdot \mathbf{U} = 0 \quad [1]$$

$$\nabla \cdot (\rho \mathbf{U}\mathbf{U}) = -\nabla p + \mu \nabla^2 \mathbf{U} \quad [2]$$

where $\mathbf{U}$ is the velocity vector and p is the pressure.

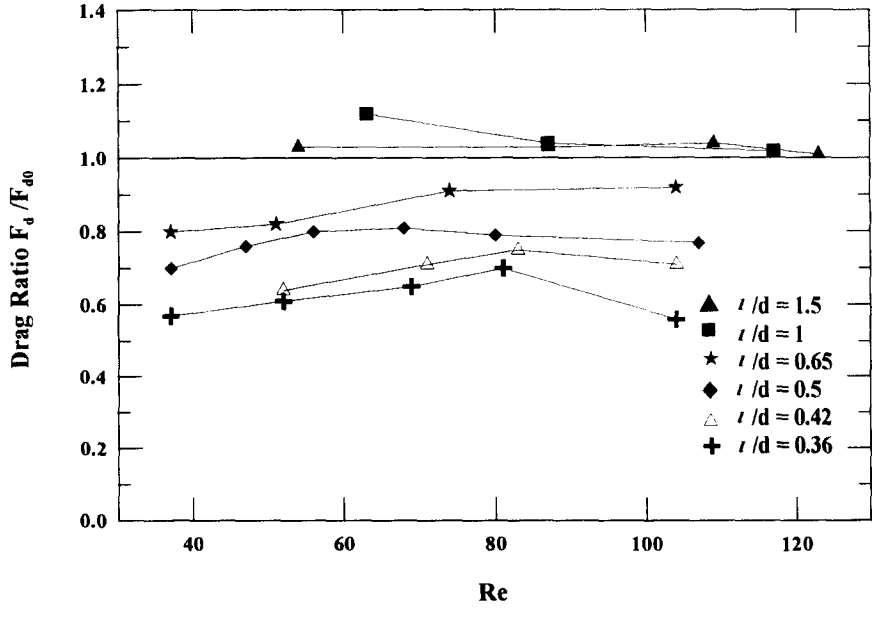

Figure 10. Variations in the drag ratio with Re for various particle separation distances for Model IV.

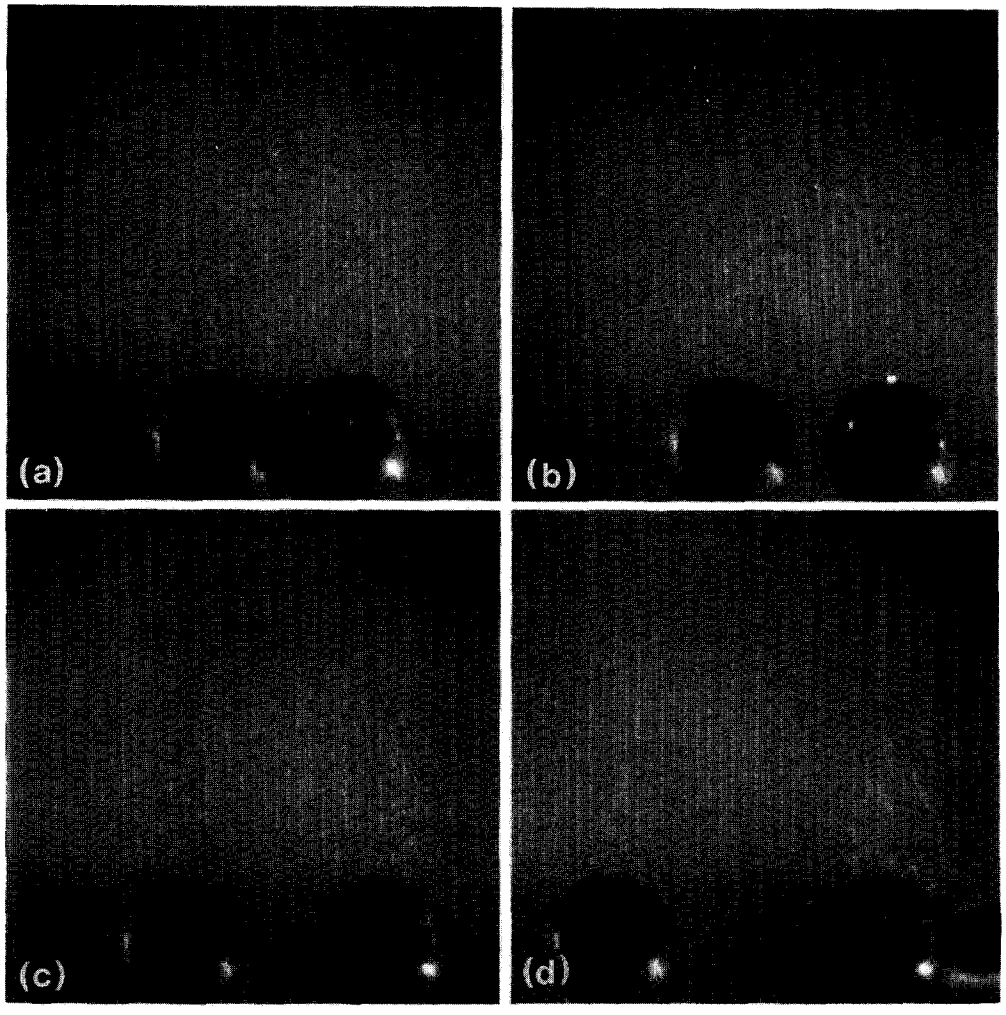

Figure 11. Wake interaction region of the two particles in Model I with $\theta = 90°$: (a) $l/d = 0$; (b) $l/d = 0.25$; (c) $l/d = 0.5$; and (d) $l/d = 1$.

To match the experimental conditions, a fully developed laminar pipe flow velocity distribution is used at the inlet boundary

$$u = u_0\left(1 - \frac{r^2}{R^2}\right) \text{ and } v = 0 \qquad [3]$$

where u_0 is the flow velocity along the pipe centerline, and u and v are the velocity components along and orthogonal to the pipe centerline, respectively. Table 2 lists the physical properties and other parameters used in the simulation, which also match the experimental conditions.

Along the centerline

$$v = 0 \text{ and } \frac{\partial u}{\partial r} = 0. \qquad [4]$$

At the particle surface and the surface of the wall, a non-slip condition is employed

$$\mathbf{U} = 0. \qquad [5]$$

At the domain outlet, it is assumed that

$$v = 0 \text{ and } \frac{\partial u}{\partial x} = 0 \qquad [6]$$

where x is the coordinate along the pipe centerline.

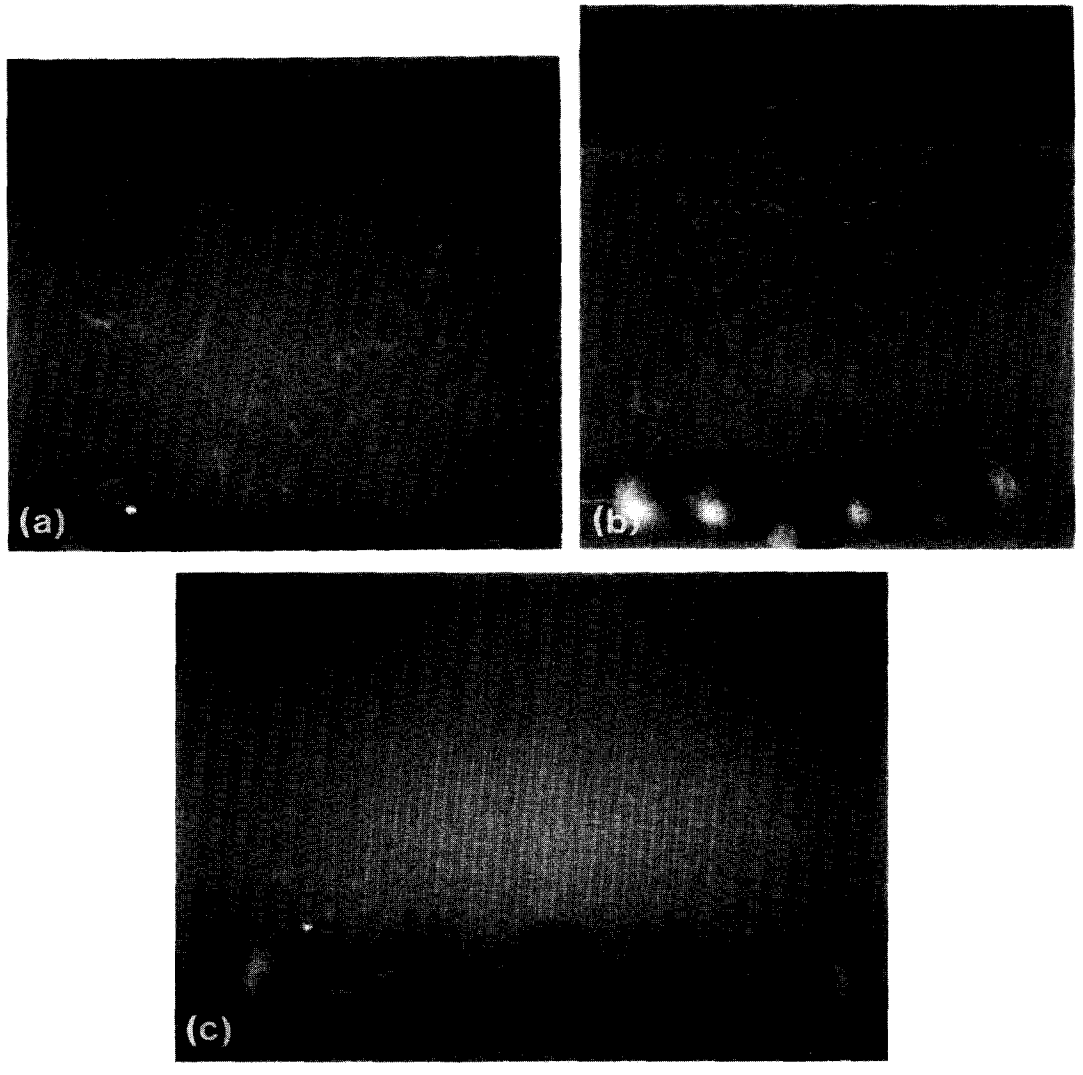

Figure 12. Wake interaction region of the six particles in Model III: (a) $l/d = 0.25$; (b) $l/d = 0.5$; and (c) $l/d = 1$.

To accurately determine wall shear stresses, a body-fitted coordinate system is adopted that better approximates the surface of the particle. A non-uniform grid system is used in order to minimize the number of grids while maintaining a sufficient degree of accuracy in the solution; very fine grids are placed at particle surfaces and wake regions. In this simulation, since the line of particle centers is also the centerline of the pipe, the problem is axisymmetric. Figure 13 shows the grid system and the computational domain for Model II for $l/d = 0.5$. The shear stress on the wall, τ_w, is calculated by assuming a linear velocity gradient adjacent to the wall:

$$\tau_w = \mu \frac{\Delta \mathbf{U}}{\Delta \mathbf{n}} \qquad [7]$$

where $\mathbf{n}$ is normal to the wall. This approximation is valid since in this simulation the near-wall

Table 2. Parameters used in the numerical simulation

ρ (g/cm^3)	μ (g/cm-s)	d (cm)	R (cm)	u_0 (cm/s) Re = 53.42	Re = 106
1.206	0.57	1.5875	7.62	16	31.6

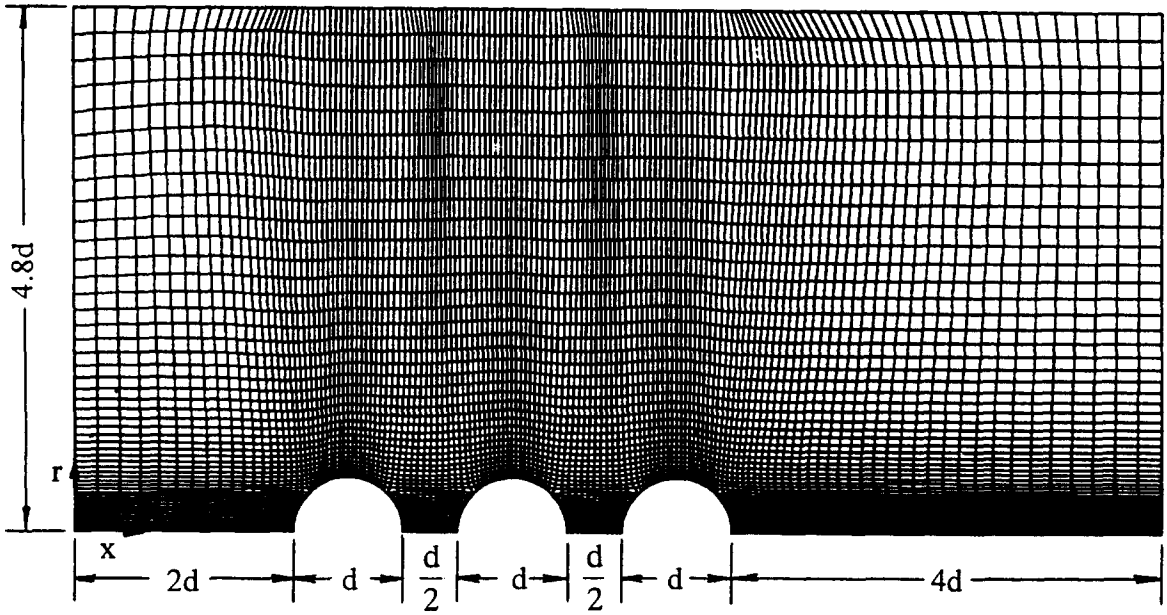

Figure 13. Grid system for Model II for $l/d = 0.5$.

grid spacing in the direction normal to the surface is chosen to be very small such that the actual flow velocity adjacent to the surface obeys a linear variation between the wall surface and the near-wall node.

The governing equations are solved using a widely accepted finite difference software package FLUENT V.4.23. A control-volume-based technique (Patankar 1980) is used to solve the conservation equations for mass and momentum. A high order discretization scheme—the QUICK scheme (Leonard 1979)—is used to overcome the numerical diffusion and obtain an accurate flow field in the wake region. The SIMPLE algorithm (Patankar 1980) is used to resolve the coupling between velocity and pressure, and the minimum dimensionless pressure residual sum is set to be 1.0×10^{-6}. A typical case study requires 8 h CPU time on a VAX 4000-90 workstation.

3.3.2. Code verification. The grid density independence of the simulation results is verified from the simulation results of a flow over a single particle for two grid densities. The drag coefficients as a function of grid density are given in table 3. The form drag coefficient, C_{dp}, and the friction drag coefficient, C_{df}, are defined as:

$$C_{dp} = \frac{F_p}{\frac{1}{2}\rho \bar{U}^2 \pi \left(\frac{d}{2}\right)^2}; \quad C_{df} = \frac{F_f}{\frac{1}{2}\rho \bar{U}^2 \pi \left(\frac{d}{2}\right)^2} \tag{8}$$

where F_p and F_f are the form drag and friction drag on the particle, respectively. It is noted that the Re in the numerical simulation is also defined based on $\bar{U}$. For a fully developed flow at

Table 3. Drag coefficients as a function of grid density for a flow passing an isolated particle

Re	$N1 \times N2$	C_{dp0}	C_{df0}	C_{d0}
53.42	37 × 27	0.704	0.893	1.596
53.42	73 × 53	0.675	0.908	1.583
106.0	37 × 27	0.590	0.552	1.142
106.0	73 × 53	0.537	0.567	1.104

Table 4. Comparison of predicted separation angle and drag coefficient for flow passing an isolated particle with those in the literature

Re	θ_{sep}		C_{d0}	
	Clift	Present work	White	Present work
53.42	137.7°	139.8°	1.567	1.583
106.0	125.6°	125.4°	1.158	1.104

Table 5. Effect of the pipe wall on the characteristic flow parameters for Model II at Re = 53.42 and l/d = 0.5

	D = 15.24 cm			D = 30.48 cm		
	Particle A	Particle B	Particle C	Particle A	Particle B	Particle C
θ_{sep}	152°	142°	130°	151°	141°	129°
C_{dp}	0.221	0.140	0.563	0.222	0.145	0.580
C_{df}	0.389	0.358	0.815	0.394	0.367	0.831
C_d	1.378	0.497	0.611	1.411	0.512	0.617

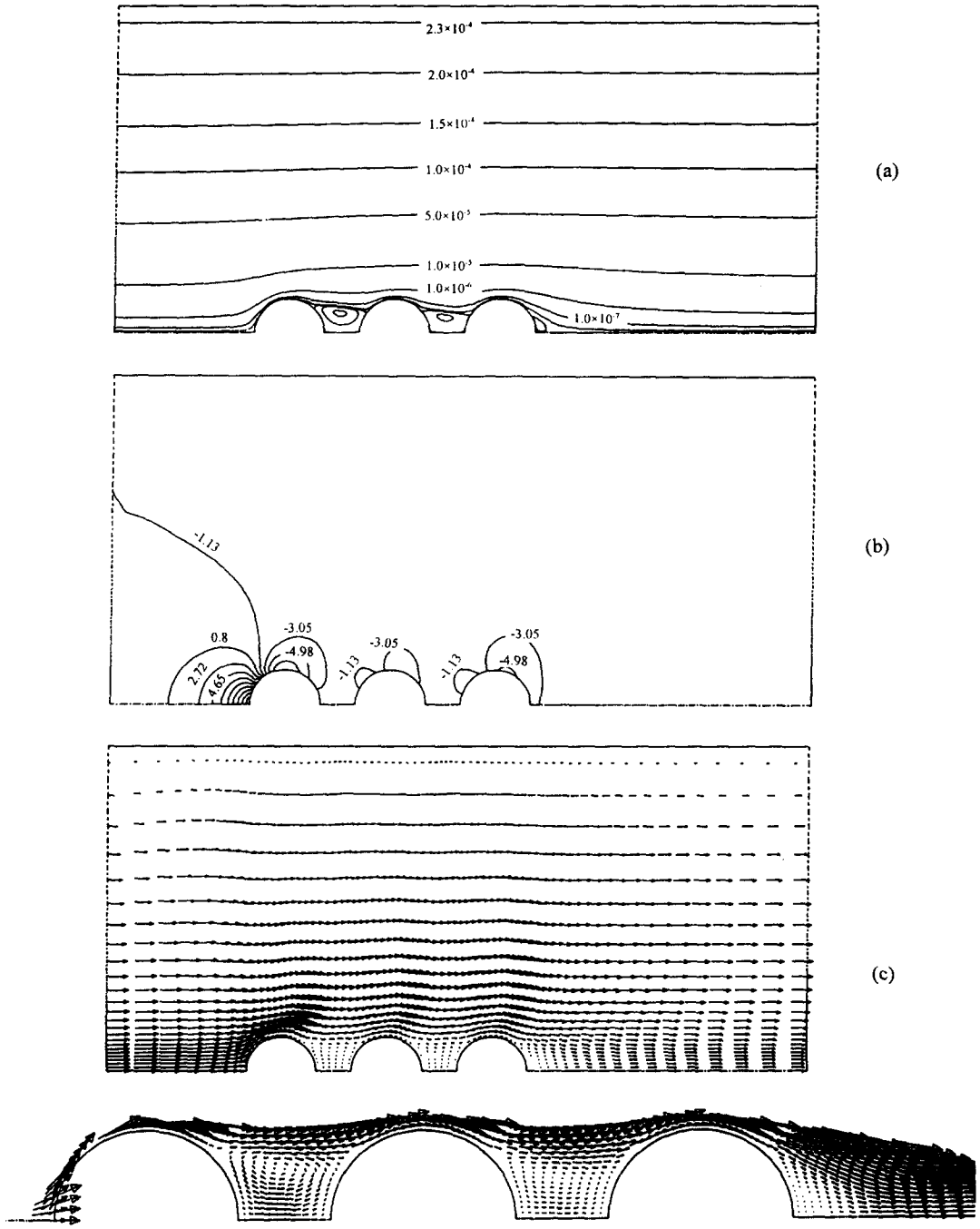

Figure 14. Streamlines (a), pressure distribution (b) and velocity vector field (c) for Model II for l/d = 0.25 and Re = 53.42.

$D/d = 9.6$, the value of $\bar{U}$ is found to be smaller than u_0 by only 0.6%. As shown in the table, for Re = 53.42 and 106, there is a very small difference in the simulated drag coefficients between the two grid densities 37 × 27 and 73 × 53. In this study, the higher grid density is employed.

The numerical code is verified by comparing the drag coefficient and separation angle of a single particle with those reported in the literature. In this study, it is assumed that the flow separates at the point where the streamwise component of the surface shear stress vanishes, and the separation angle, θ_{sep}, is measured from the forward stagnation point of the particle to the point where the flow separates. The wake length is measured from the particle surface to the point where the axial velocity component along the symmetric axis vanishes. As shown in table 4, the simulated results agree very well with those reported by Clift (1978) and White (1974).

3.3.3. Effect of the pipe wall. To investigate the effect of the pipe wall, simulations for two different pipe diameters, 15.24 and 30.48 cm, at $u_0 = 16$ cm/s and $l/d = 0.5$ are conducted under the same boundary conditions. Because the flow velocity profiles at the inlet boundary in both cases are based on the same value of u_0, the Re based on $D = 30.48$ cm is slightly higher than the Re based on $D = 15.24$ cm by 0.3%. The predicted flow parameters are given in table 5. The results show that as the D/d increases from 9.6 to 19.2, no significant changes in the characteristic flow parameters are observed; the slightly higher drag coefficients for $D/d = 19.2$ result from the slight increase in the average flow velocity, $\bar{U}$. This indicates that for Model II the effect of the pipe wall is insignificant and the results obtained in this study can be expanded to an unbounded flow.

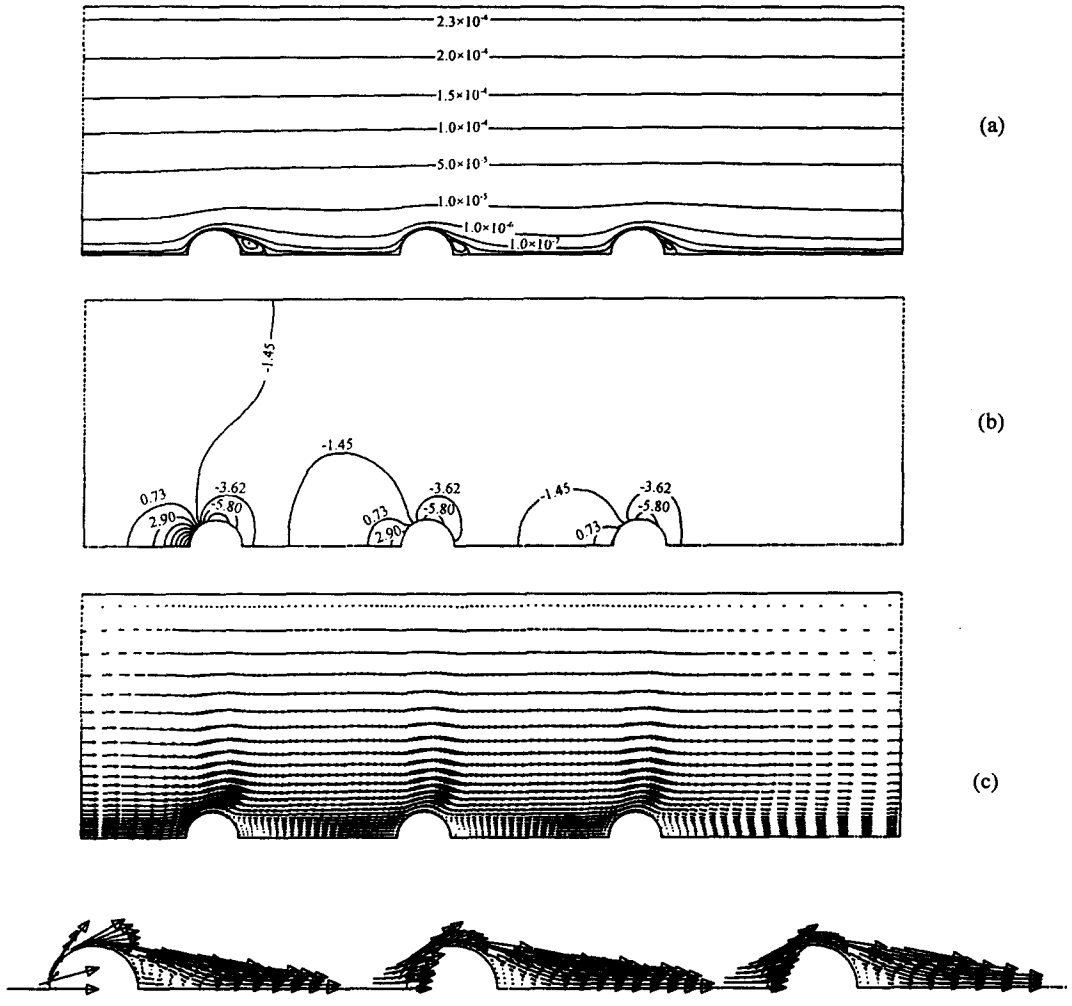

Figure 15. Streamlines (a), pressure distribution (b) and velocity vector field (c) for Model II for $l/d = 3.0$ and Re = 53.42.

Table 6. Separation angles and wake lengths for Model II at Re = 53.42

	l/d	θ_{sep}	l_w/d	l_w/l_{w0}
Particle C	0.25	129°	†	†
Particle B	0.25	141°	†	†
Particle A	0.25	153°	0.157	0.367
Particle C	0.5	130°	†	†
Particle B	0.5	142°	†	†
Particle A	0.5	152°	0.165	0.386
Particle C	3.0	140°	0.472	1.103
Particle B	3.0	144°	0.308	0.720
Particle A	3.0	148°	0.231	0.540

†The wake fills the entire gap between the two particles.

3.3.4. Flow structures. Figure 14(a)–(c) shows the streamlines, pressure contours and velocity vector distribution, respectively, around the three particles for $l/d = 0.5$ and Re = 53.42. The corresponding flow fields for $l/d = 3$ are shown in figure 15(a)–(c). The streamlines and the velocity field show clearly the onset of flow separation and the wake structures. The pressure contours show that the pressure variation on the surface of particle C is much larger than that of particles A and B, which leads to larger form drag for particle C.

The separation angles and the wake lengths of all three particles for $l/d = 0.25$, 0.5 and 3 at Re = 53.42 are listed in table 6. The term l_w is the wake length for Model II, and l_{w0} represents that of the single particle case. It is found that the separation angle decreases and the wake length increases with the particle order A, B, C. Because of the close spacing for $l/d = 0.25$ and 0.5, the wakes of particles C and B fill the gaps between particles C and B, and A and B, respectively; a second separation point occurs on the front portion of particles A and B. The flow separation on the rear portion of the particle is accelerated for particle C and delayed for particles A and B when compared with a single particle. For $l/d = 3$, the wake lengths of particles A and B are less than that of a single particle but the wake length of particle C is 1.1 times larger than that of a single particle. The flow separation angle of particle C is found to be almost the same as that of a single particle.

3.3.5. Drag coefficients and drag ratios. Table 7 shows the form, friction and total drag coefficients and their ratios for each particle at three separation distances at Re = 53.42. The information of C_{dp} and C_{df} are important since it is an indicator of the importance of one relative to the other. The term C_{d0} represents the numerically simulated drag coefficient of a single particle. It should be noted that the drag coefficient ratio C_d/C_{d0} is identical to the drag ratio F_d/F_{d0}. As shown in table 7, there is a good agreement between the experimentally determined and numerically simulated total drag ratios. It is found that, in general, the values of C_{dp}, C_{df} and C_d for all three particles increase with increasing separation distance. Because the value of C_{dp} increases faster than that of C_{df}, the form drag contribution to the total drag for all three particles also increases. As the l/d increases from 0.5 to 3, both the values of C_{dp} and C_{df} for particle B increase faster than those for particle A, which leads to the change in the drag ratio order for particles A and B as observed in experiments. This phenomenon can be seen more clearly in figures 16 and 17. It can also be seen that the reason for the drag ratio of particle B to be much less than unity is

Table 7. Drag coefficients for Model II at Re = 53.42

	l/d	C_{dp}	C_{df}	C_d	C_d/C_{d0}	C_d/C_{d0} experimental
Particle C	0.25	0.564	0.811	1.375	0.894	0.90
Particle B	0.25	0.104	0.334	0.437	0.284	0.26
Particle A	0.25	0.199	0.372	0.571	0.371	0.39
Particle C	0.5	0.563	0.815	1.378	0.896	0.91
Particle B	0.5	0.140	0.358	0.497	0.323	0.31
Particle A	0.5	0.221	0.389	0.611	0.397	0.41
Particle C	3.0	0.649	0.878	1.527	0.993	0.97
Particle B	3.0	0.374	0.559	0.933	0.607	0.60
Particle A	3.0	0.336	0.505	0.841	0.547	0.59

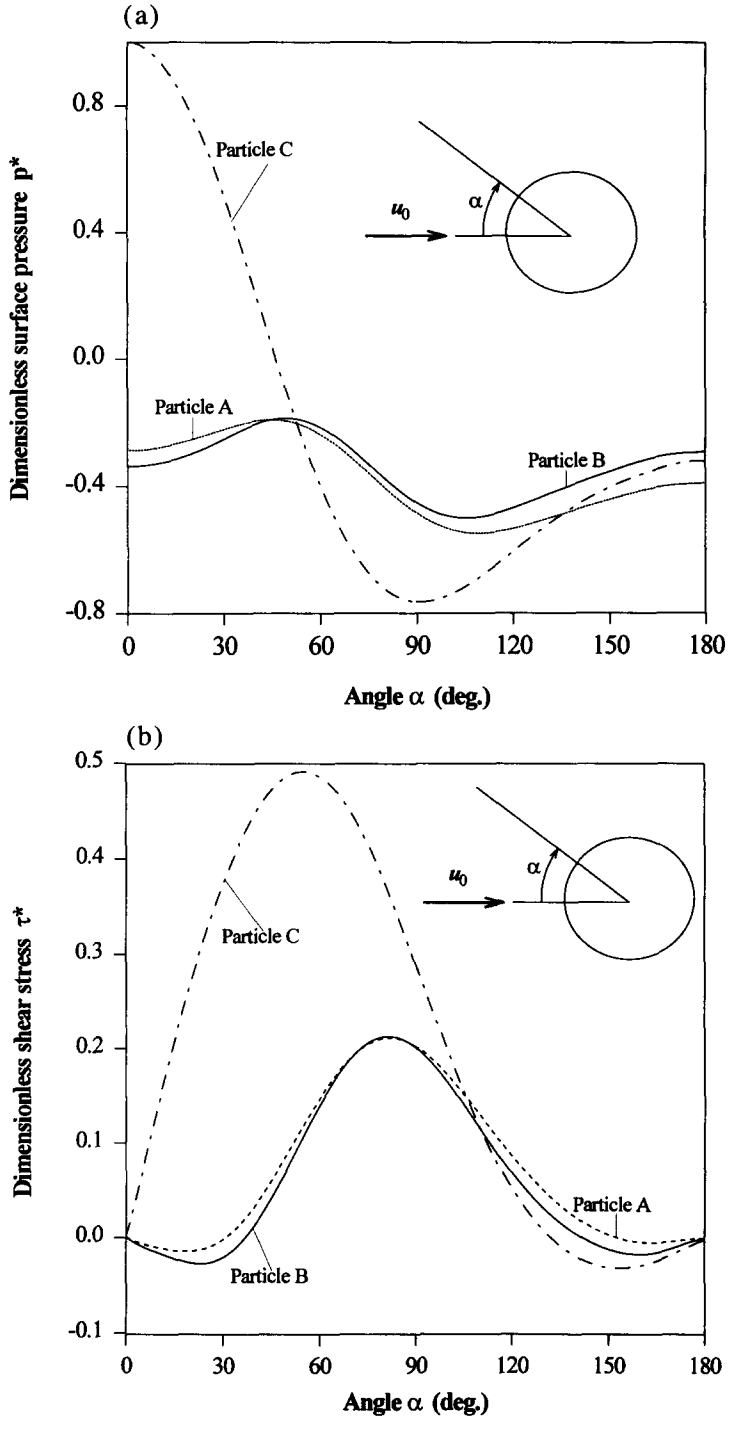

Figure 16. Distributions of the pressure (a) and the shear stress (b) on the surface of the three particles for Model II for l/d = 0.5 and Re = 53.42.

because there is a very significant reduction in the form drag. The form drag of particle B for l/d = 0.25 reduces to 15% of that of a single particle while the friction drag reduces to 37% of that of a single particle.

3.3.6. Surface pressure and shear stress distributions. Figures 16(a) and 17(a) show the distribution of the dimensionless surface pressure, $p^*(=2(p_s - p_0)/\rho\bar{U}^2)$, on the particle surface for l/d = 0.5 and 3, respectively. The Re is 53.42 for both cases. The term p_s represents the pressure at the

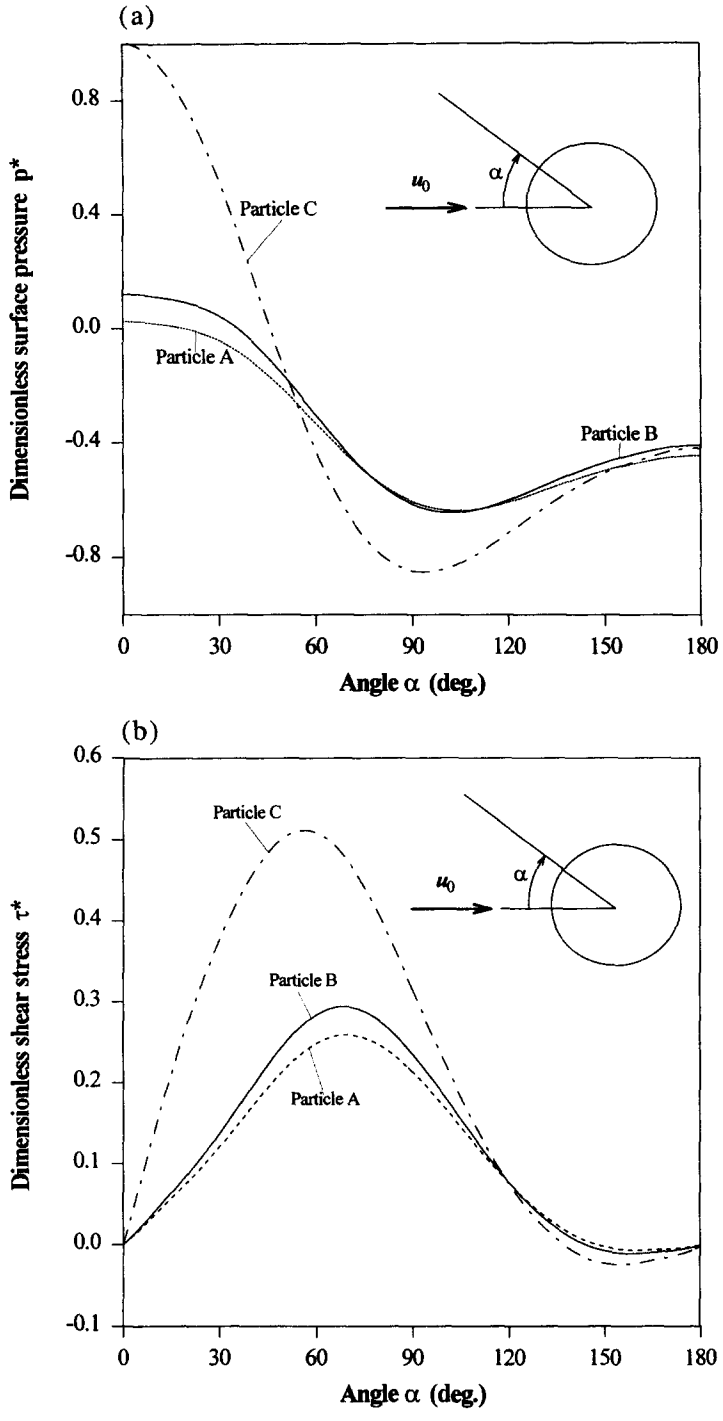

Figure 17. Distributions of the pressure (a) and the shear stress (b) on the surface of the three particles for Model II for l/d = 3.0 and Re = 53.42.

particle surface, p_0 represents the pressure at the forward stagnation point of particle C and α represents the angle from the pipe centerline. It can be seen that the pressure distribution on the surfaces of particles A and B are similar; the p^* for particle C is much higher than those for particles A and B for small values of α, but the difference in the p^* among the three particles is much less significant for larger values of α. This is the reason why particle C has the highest form drag coefficient. For l/d = 3, the flow fields around particles A and B more closely resemble that

of a single particle; therefore, the difference in p^* between particles A and B and particle C is reduced. Figures 16(b) and 17(b) show the distribution of the dimensionless surface shear stress, $\tau^*(=2\tau_w/\rho\tilde{U}^2)$, on the particle surface for $l/d = 0.5$ and 3, respectively. It is found that the τ^* of all three particles are positive except in the wake regions, and the τ^* of particle C is much higher than those of particles A and B at small α. For $l/d = 0.5$, negative values of the τ^* are found for particles A and B at small α, which are induced by the wakes of particles B and C, respectively.

4. CONCLUDING REMARKS

The single particle drag force is measured under conditions where the test particle is surrounded by other equal-sized particles arranged in four different configurations: a two-particle configuration, a three-coaligned particle configuration, a hexagonal particle configuration and a cubic particle configuration. The drag ratio, defined as the ratio of the drag force of the test particle to that of an isolated particle, is evaluated by considering the effects of five variables including: the number of surrounding particles, the distance between particles, relative positions of the particles, the Re and the presence of pipe wall. For the two-particle configuration, the symmetry of the drag ratio with respect to $\theta = 90°$ for the Stokes flows is found to be distorted because of both the Re and wall effects. At $\theta = 90°$, the drag ratio increases with increasing Re at a given separation distance; furthermore, its values increase with separation distance and then decrease with further increasing separation distance. The concave part of the drag ratio curves appears to flatten out as the Re further increases. For the three-coaligned particle configuration, the drag ratio of particle B is larger than that of particle A for l/d of about 2–3. The sum of the drag ratios of the three particles is lower than that obtained for the Stokes flow conditions. For the hexagonal particle configuration, an increase in the drag ratio of up to 40% is observed at a separation distance of 0.5 and Re = 71. For the cubic particle configuration, the drag ratio is found to be generally less than unity and the Re does not seem to affect the drag ratio for all separation distances investigated. The flow visualization of Models I and III reveals that as the separation distance becomes very small, a single particle vortex-ring formed in the wake region of the particle assembly. The simulation results on Model II agree reasonably well with the experimental results. The detailed flow field information clearly demonstrates the variation in the flow structure around a particle due to the presence of other particles. The pressure and shear stress distributions on the particle surfaces provide physical insight into the drag ratio behavior observed in this study.

Acknowledgement—This work was supported by the NSF grant CTS-9200793.

REFERENCES

Ayukawa, K., Ochi, J. & Shinmyo, S. 1970 The effects of wall and concentration on the terminal velocities of solid particles. *Bull. JSME* **13,** 996–1004.

Brady, J. & Bossis G. 1988 Stokesian dynamics. *A. Rev. Fluid Mech.* **20,** 111–157.

Batchelor, G. K. 1982 Sedimentation in a dilute polydisperse system of interacting spheres. Part I. General theory. *J. Fluid Mech.* **119,** 379–408.

Clift, R. 1978 *Bubbles, Drops, and Particles*. Academic Press. New York.

Fuentes, Y. O. & Kim, S. 1992 Parallel computational microhydrodynamics: communication scheduling strategies. *AIChE J.* **38,** 1059–1078.

Ganatos, P., Pfeffer, R. & Weinbaum, S. 1978 A numerical-solution technique for three-dimensional Stokes flow, with application to the motion of strongly interacting spheres in a plane. *J. Fluid Mech.* **84,** 79–111.

Goldman, A. J., Cox, R. G. & Brenner, H. 1966 The slow motion of two identical arbitrarily oriented spheres through a viscous fluid. *Chem. Engng Sci.* **21,** 1151–1170.

Happel, J. & Brenner, H. 1983 *Low Reynolds Number Hydrodynamics*. Prentice-Hall, Englewood Cliffs, NJ.

Happel, J. & Epstein, N. 1954 Cubical assemblages of uniform spheres. *Ind. Engng Chem.* **46,** 1187–1194.

Jaiswal, A. K. & Sundararajan, T. 1991 Flow characteristics of settling suspensions and fluidized beds of spherical particles. *Chem. Engng Commun.* **106,** 139–149.

Kim, I., Elghobashi, S. & Sirignano, W. A. 1993 Three-dimensional flow over two spheres placed side by side. *J. Fluid Mech.* **246,** 465–488.

Kim, S. 1987 Stokes flow past three spheres: an analytic solution. *Phys. Fluids* **30,** 2309–2314.

LeClair, B. P. & Hamielec, A. E. 1968 Viscous flow through particle assemblages at intermediate Reynolds numbers. *I and EC Fundam.* **7,** 542–549.

Lee, K. C. 1979 Aerodynamic interaction between two spheres at Reynolds numbers around 10^4. *Aeronaut. Q.* **30,** 371–385.

Leonard, B. P. 1979 A stable and accurate convective modeling procedure based on quadratic upstream interpolation. *Computer Meth. Appl. Mech. Engng.* **19,** 59–98.

Patankar, S. V. 1980 *Numerical Heat Transfer and Fluid Flow*. Hemisphere, Washington, DC.

Ramachandran, R. S., Wang, T.-Y., Kleinstreuer, T. & Chian, H. 1991 Laminar flow past three closely spaced monodisperse spheres or nonevaporating drops. *AIAA J.* **29,** 43–51.

Richardson, J. F. & Meikle, R. A. 1961 Sedimentation and fluidisation—Part IV: drag force on individual particles in an assemblage. *Trans. Inst. Chem. Engrs* **39,** 357–362.

Rowe, P. N. 1961 Drag forces in a hydraulic model of a fluidised bed–part II. *Trans. Inst. Chem. Engrs* **39,** 175–180.

Rowe, P. N. & Henwood, G. A. 1961 Drag forces in a hydraulic model of a fluidized bed–part I. *Trans. Inst. Chem. Engrs* **39,** 43–54.

Schlichting, H. 1979 *Boundary-layer Theory*, 7th Edn. McGraw–Hill, New York.

Soo, S. L. 1990 *Fluid Dynamics of Multiphase Systems*. Science Press, Beijing, China.

Stinzing, H. D. 1971 Fluid drag on clouds consisting of solid particles enclosed in a pipe. *Proc. 1st Int. Conf. on the Pneumatic Transport of Solids in Pipes*, Paper C6.

Tal, R., Lee, D. N. & Sirignanao, W. A. 1984 Heat and momentum transfer around a pair of spheres in viscous flow. *J. Heat Mass Trans.* **27,** 1953–1962.

Taniguchi, I. & Asano, K. 1987 Numerical analysis of drag coefficients and mass transfer of two adjacent spheres. *J. Chem. Engng Japan* **20,** 287–294.

Tsuji, Y., Morikawa Y. & Fujiwara, Y. 1985 Pipe flow with solid particles fixed in space. *Int. J. Multiphase Flow* **11,** 177–188.

Tsuji, Y., Morikawa, Y. & Terashima, K. 1982 Fluid-dynamic interaction between two spheres. *Int. J. Multiphase Flow* **8,** 71–82.

White, F. M. 1974 *Viscous Fluid Flow*. McGraw–Hill, New York.

Zhu, C., Liang, S.-C. & Fan, L.-S. 1994 Particle wake effects on the drag force of an interactive particle. *Int. J. Multiphase Flow* **20,** 117–129.